Supplementary Information

We divide the supporting information into Supplementary figures, Supplementary Methods and four notes that cover (1) the Brownian noise and phase slippage; (2) the role of the distance to the wall and the angle δ in the state of synchronization; and finally, the details of (3) the analytical calculations and (4) the numerical simulations that support the experimental data.

Supplementary Figures

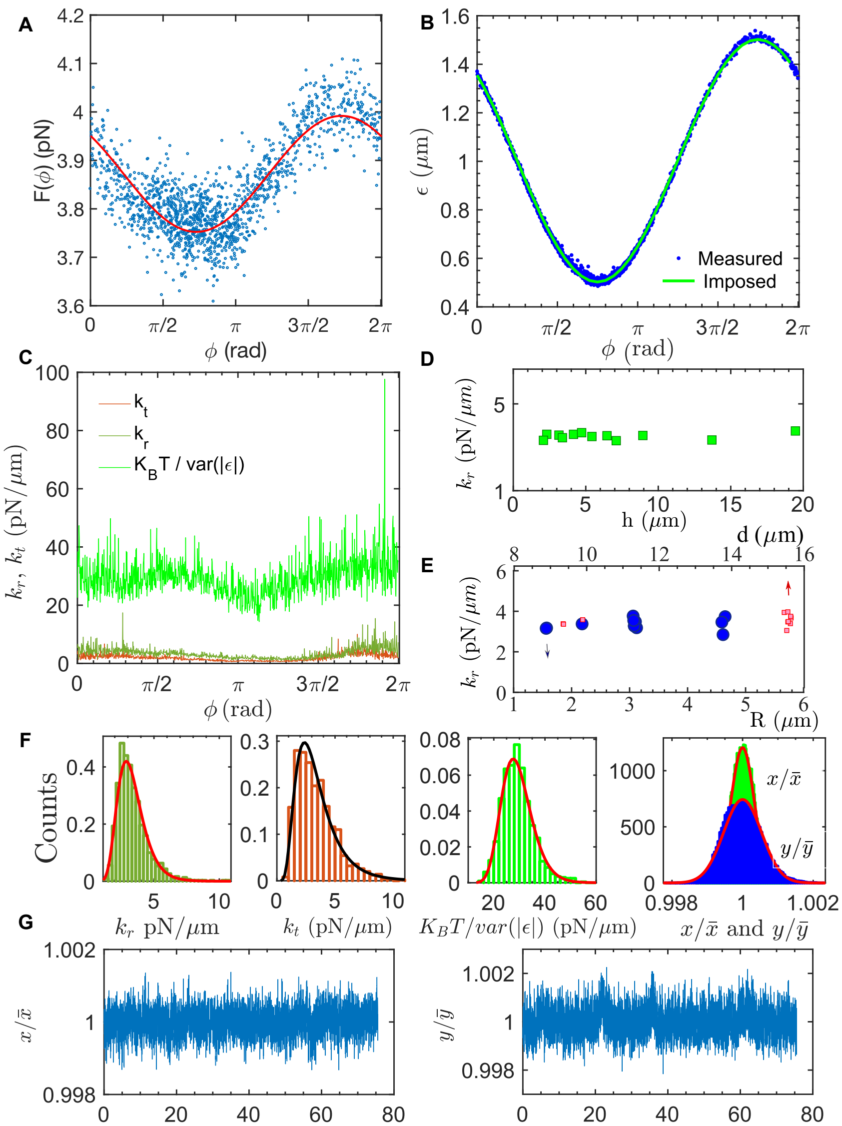

Supplementary figure 1: Calibration of a single rotor. (a) (o) Measured driving force acting on a single colloidal particle according to $F(\phi) = 6\pi\eta a v(\phi)$, where $v(\phi) = 2\pi R(\phi)/T_0$ with R the radius of the orbit and T_0 the period. (–) The imposed force $F(\phi) = F_0\,[1 + A\sin(\phi + \delta)]$, with $A = 0.5$ and $\omega = 3\pi/4$, is also plotted for comparison. Each rotor is experimentally implemented by using feedback-controlled optical tweezers, in which the position of the trap is updated based on the position of the particle (o), and maintained a distance $\epsilon(\phi)$ along the trajectory tangent, ahead of the particle, as shown in (b). Here, (–) represents imposed and (o) measured ϵ. (c) From the analysis of the fluctuations in the radial and tangential directions it is shown that the trapping force is a harmonic potential with spring constants k_r and k_t in each direction respectively. $k_r = k_t$ are independent of ϕ. For the sake of comparison we also plotted here the fluctuations of ϵ, $K_BT/var(|\bar{\epsilon}|)$. In this particular run, the average radial stiffness $\langle k_r \rangle = 3 \pm 1\,\mathrm{pN}/\mu\mathrm{m}$ does not depend on the distance to the wall h (d), the radius of the orbit R, or the distance between rotors d (e). In (f) we show the distribution of stiffness of a single rotor. The Gaussian fits (lines) match the experimental data very well. (g) Fluctuations in the x, y directions of an individual trapped particle, In (f), also the fluctuations in both directions follow a Gaussian fit.

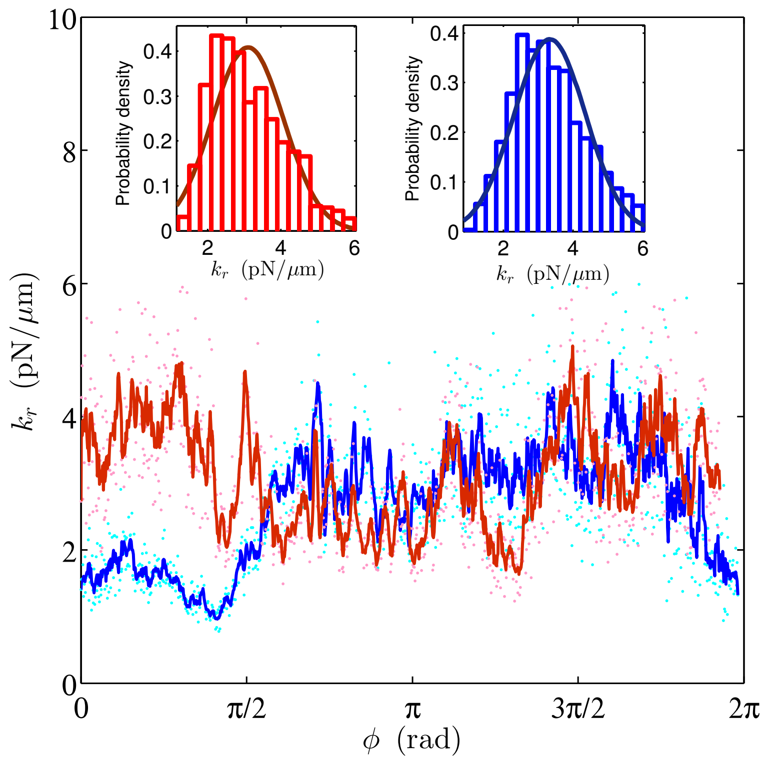

Supplementary figure 2: Radial stiffness k_r measured as a function of the phase ϕ for a single rotor for different values of force modulation: A=0.5 (red), and 0.7 (blue). The trapping force along the radial direction is approximated by an harmonic potential with a spring constant that is independent of ϕ. The inset show the distribution of the radial stiffness of a single rotor for the two values of A considered. The Gaussian fits (lines) match the experimental data very well.

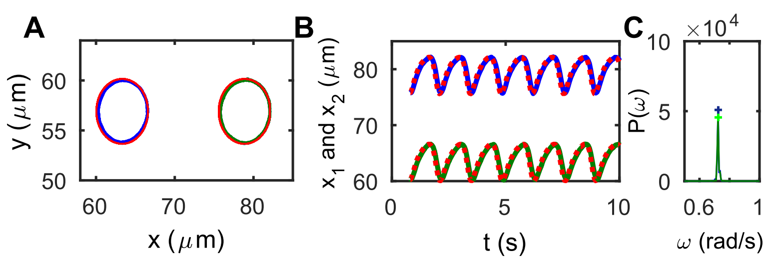

Supplementary figure 3: Calibration of a pair of rotors. (a) Two driven particles along circular orbits –particles (o, o) and traps (o)– in an experiment with $R = 3.17\,\mu$m and $d = 15.85\,\mu$m. (b) Displacement of the particles projected on x-axis. (c) The power-spectrum of the positions of the two particles during the experiment from which $\omega_0 (= 2\pi/T_0)$ is obtained. We calibrated the particle trajectories in such a way that their intrinsic rotation period T_0 matches to better than 5%.

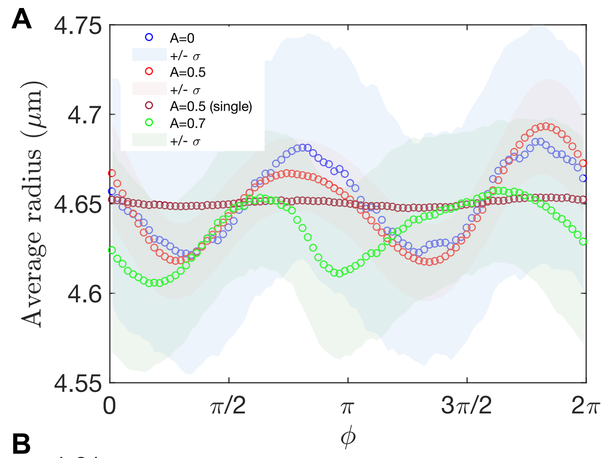

Supplementary figure 4: Panel (a) shows the average radius of the orbit that corresponds to Rotor 1 in isolation $R_{1,0}$ and R_1 when a second Rotor describing also a similar trajectory is present for a simulated experiment with $A = 0.5$. The average radius for $A = 0.7$ and constant force modulation, $F(\phi) = F_0$, with $A = 0$ are also plotted. Shaded error bars correspond to the standard deviation. The rest of parameters are $R = 4.65\ \ \mu$m, $d = 15.85\,\mu$m, $h = 10\,\mu$m, and $\delta = 3\pi/4$. We used $k_r = 3\,$pN$/\mu$m in all the cases. (b) corresponds to the comparison of the ratio $< R_1 > / < R_{1,0} >$ for A=0, A=0.5 and A=0.7.

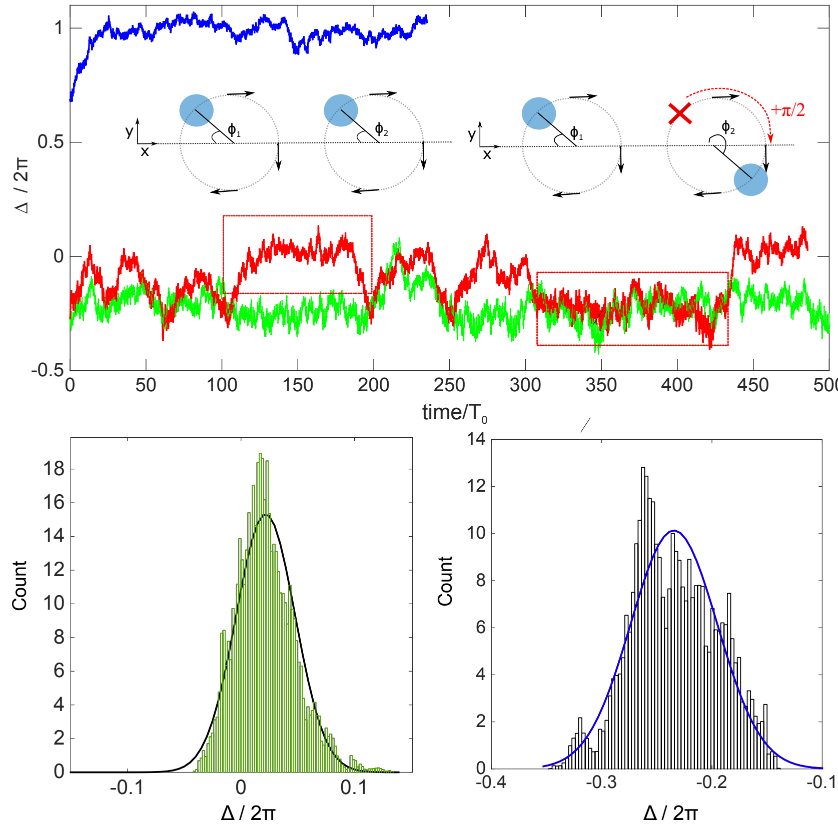

Supplementary figure 5: Example of stochastic switching between IP and OP locked states: (Top) Normalised phase difference $\Delta/2\pi$ plotted against normalised time t/T_0. Experimental details are $R = 4.6$ μm, with $d = 15.85\,\mu$m; Distance to the wall was fixed to $h = 30\,\mu$m. Force profiles parameters are: $A = 0.5$ (blue), 0.6 (red), and 0.7 (green) with $\delta = 3\pi/4$ in all the cases. For $A = 0.5$, the two rotors shows IP locking ($\Delta \approx 2\pi$), while $A = 0.7$ leads to OP locking ($\Delta \approx -\pi/2$) during the 500 cycles ($\approx$1500 s) of the experiment. For $A = 0.6$, the system shows stochastic transitions between IP and OP driven by thermal noise (see e.g. the regions highlighted in rectangles). Within the two highlighted IP and OP regions, Δ follows a Gaussian distribution (bottom histograms).

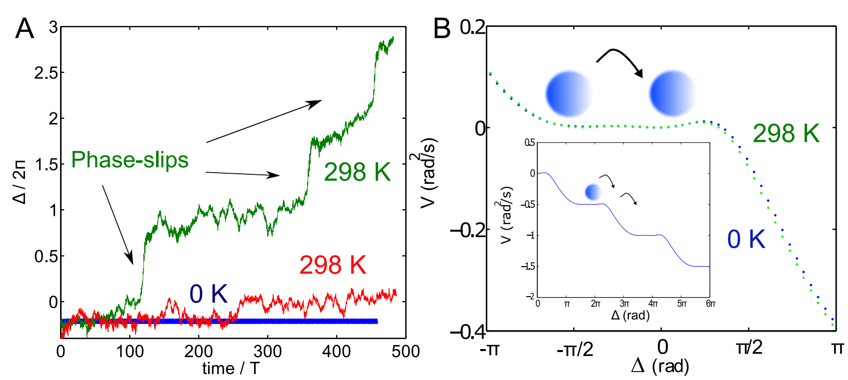

Supplementary figure 6: (a) Normalised phase difference $\Delta/2\pi$ plotted against normalised time t/T_0 for three different runs. Data obtained with simulations with the experimental parameters: $R = 4.6$ μm, and $d = 15.85\,\mu$m; Distance to the wall was fixed to $h = 30\,\mu$m; and the amplitude $A = 0.6$. (b) Effective potential at $T = 0$, and 298 K. Inset: Effective potential at 298K in a more wider region of Δ to show how the noise can lead to stochastic transitions between adjacent minima of the tilted potential $V(\Delta)$.

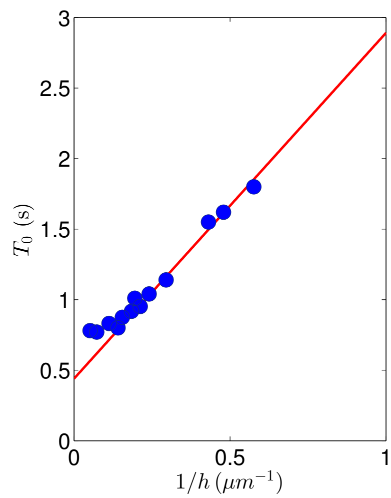

Supplementary figure 7: Intrinsic period of rotation T_0 of a colloidal particle describing a circular trajectory versus the inverse of the distance to the wall h. Straight line shows the linear dependence of the experimental data.

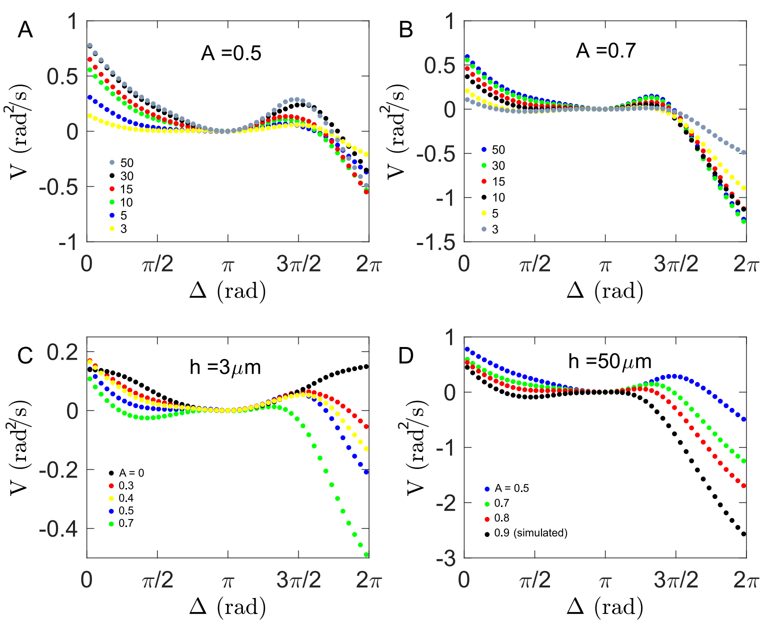

Supplementary figure 8: Effective potentials $V(\Delta)$ obtained from optical tweezers experiments (except in (d), for which the potential at $A = 0.9$ is obtained by numerical simulation because it was experimentally not accessible). Parameters are $R = 4.6\ \mu$m, and $d = 15.85\,\mu$m. Both h and A are varied with $\delta = 3\pi/4$ constant. (a,b) Influence of h for two different modulation parameter A. (c,d) Effect of the variation of A in the shape of the potential for the two limiting cases $h = 3$ and $50\,\mu$m.

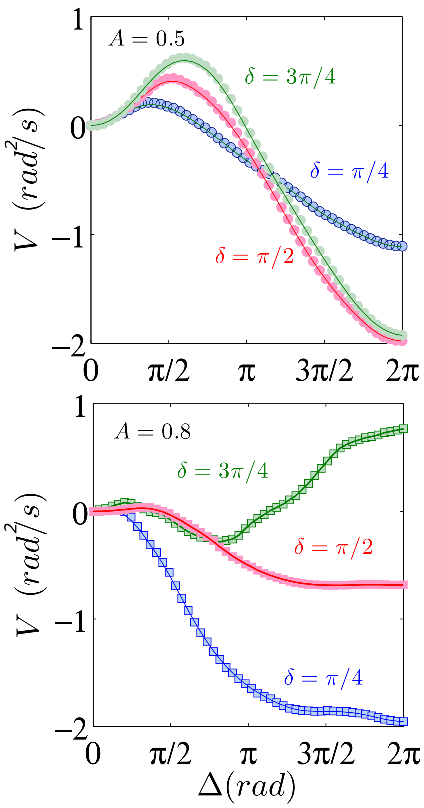

Supplementary figure 9: Effective Potential $V(\Delta)$ at different values of δ. Two different modulation parameters are been considered, $A = 0.5$ for which IP locked-state is observed independly of δ; and $A = 0.8$, for which $\delta = 3\pi/4$ clearly leads to OP synchronisation, while $\delta = \pi/4$ and $\pi/2$ show two minima, in which hopping events due to Brownian noise are observed.

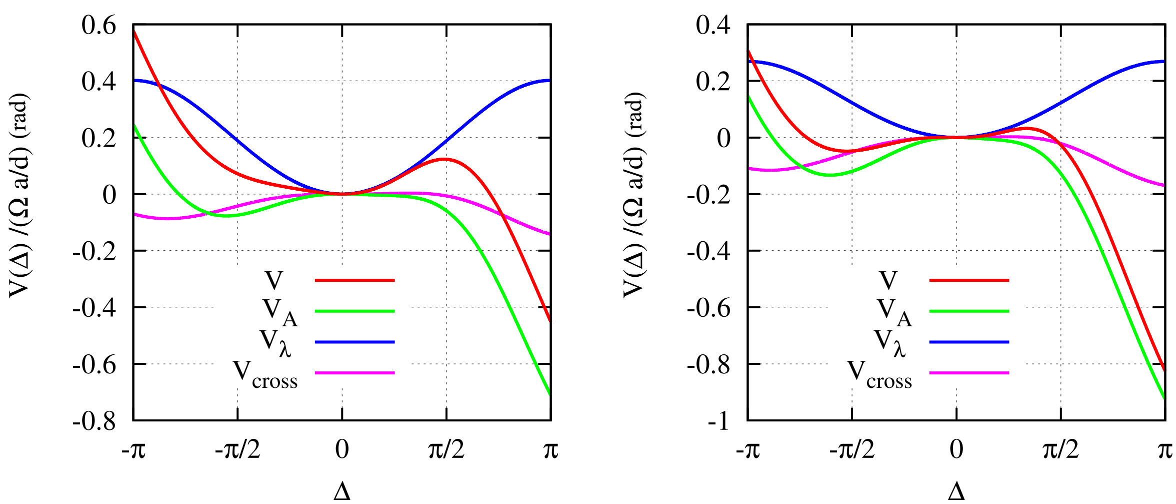

Supplementary figure 10: Potential Decomposition: (left) IP and (right) OP. Each is obtained from the theoretical potential in the top and bottom panel of Fig.3, respectively.

Supplementary Methods

Experiment concept

The rotors with circular trajectories of radius R are implemented by using a feedback-controlled force driving, in which the position of each trap is updated based on the instantaneous position of that particle and the pre-determined orbit geometry. The traps are always maintained at a distance $\epsilon(\phi)$ ahead of the projection of the position of the particle on the predefined trajectory (Supplementary figure. 1b). The optical force acting on the particle i is

$$\mathbf{F}_i = \mathbf{F}_{i,t} + \mathbf{F}_{i,r} = k_t \epsilon(\phi_i)\hat{\mathbf{e}}_{t,i} - k_r(R_i - R)\hat{\mathbf{e}}_{r,i}\,. \tag{S1}$$

The tangential component $\mathbf{F}_{i,t}$ maintains the driving force of the particles, whilst the radial component $\mathbf{F}_{i,r}$ is a restoring force that tends to keep the particles on the circular trajectory of radius R. Hence, $k_t\epsilon(\phi_i)$ defines the driving force and k_r the flexibility. In our setup, by using simple harmonic traps, $k_r \approx k_t \approx k$ as we demonstrate in section 1.4.

Setup and calibration steps

Our experiment is built around a Nikon inverted Eclipse Ti-E microscope, using a water-immersion objective (Nikon Plan Apo VC 60x, NA = 1.20). Images are taken at a rate of 230 frames per second using a CMOS camera (AVT Marlin F-131B). A time-shared trapping laser based on acoustic-optical deflection (AOD) of a beam is used to update the position of an optical trap based on the position of the particle. The laser used is a diode-pumped solid-state laser (CrystaLaser IRCL-2W-1064, with a wavelength of 1.064 μm).

A first calibration step purely concerns the optical setup. First, the frame of reference of the camera and the frame of the trap positions are calibrated to correct the position-dependent discrepancy between the measured bead position and the trap centre by measuring the position of a bead in the camera frame for different x and y positions of a trap (typically on a 20×20 grid covering the 63 μm-sized square area of available trap positions). Second, a calibration of the parameter that controls the intensity of a trap (hence the trap stiffness k), the *gain*, is done. The gain is linearised so that it becomes proportional to the measured intensities after the AOD. In addition, when changing the position of the trap (by changing the driving frequency of the AOD), the intensity can also vary, and the gain is furthermore calibrated so that it becomes independent of the position, by measuring the intensity in a grid of x and y positions of the trap (in the available trapping region).

Feedback-controlled mechanism

In a feedback loop, we analyse in real time the position of the beads and send commands to the electronics that controls the traps' positions. The analysis of the images is done by a computer at the rate of the camera. In our experiments, images are taken at a rate of 230 frames per second (fps), and each trap position is updated at the same frequency. In considering the feedback timing, one aspect is this sampling frequency. However there is also a delay in the transmission of the images to the computer, in processing, and (most significantly) in the computer transmitting new control commands to the laser beam steering electronics. The total delay is estimated to $\tau_f = 5 \pm 0.1\,\mathrm{ms}$ and is in most part due to the latency times of the computer OS in addressing the USB port. This time is always shorter than the relevant timescales in our model, in particular the relaxation time of the particle in the trap $\tau = \gamma/k \approx 65\,\mathrm{ms}$, the period of the rotors (0.7 to 1.8 s) and the timescale to synchronize.

Control of the forces on the orbits

Prior to studying the coupling between two rotors it is very important to ensure that the individual orbiting rotors follow the tangential force defined by $F(\phi) = F_0[1+A\sin(\phi+\delta)]$ with good precision. As we stated earlier a first set of calibration steps concerns purely the optical setup. Then, each rotor is calibrated in isolation in every experiment to account for imperfections in the colloidal particles. Subsequently, the values of $\epsilon_0(= F_0/k_t)$ are fine-tuned for each rotor, in such a way that both particles have the same intrinsic period of rotation. For typical values of $\epsilon_0 = 0.935 \pm 0.005\,\mu\mathrm{m}$, the precision in the measured period is better than 0.04 s, with periods T_0 typically ranging from 0.7 to 1.8 s. Supplementary figure. 1(a) shows the outcome of this experimental step, and the particle-trap distance $\epsilon(\phi)$ agrees well with the imposed function $\epsilon(\phi)$, as shown in Supplementary figure 1(b). We also observed that the intrinsic period of rotation T_0 depends linearly on inverse h, due to an increase in drag as h is reduced (see Supplementary figure 3).

The optical trap is expected to behave as an isotropic harmonic potential, so the trapping stiffness along the radial direction k_r should be the same as k_t. This can be checked by measuring the amplitude of particle radial and tangential fluctuations: to do this, for each angle the radial stiffness is measured as $k_r = k_\mathrm{B}T/\mathrm{var}(r(\phi))$, with $\mathrm{var}(r(\phi))$ the variance of the radial position at a given angle. The tangential stiffness is thus measured as $k_t = k_\mathrm{B}T/\mathrm{var}(\mathbf{R}(t)) - \mathbf{T}(t-\delta t))$, with $\mathbf{R}$ the position of the particle at a given time and $\mathbf{T}$ the position of the trap, with a delay $\delta t = 10$ frames to be outside the feedback-constraint. Supplementary figure 1(c) shows that k_r and k_t are comparable over all angles; in this particular case both fluctuates with an average value of $3 \pm 1\,\mathrm{pN}/\mu\mathrm{m}$.

We also plot here the amplitude of fluctuations of ϵ at each angle, calculated as $k_\mathrm{B}T/\mathrm{var}(|\epsilon(\phi)|)$, with $\mathrm{var}(|\epsilon(\phi)|)$ being the variance of the particle-trap distance at a given angle. There is one order of magnitude of difference between the radial and tangential stiffness and the stiffness in the feedback-controlled interval. The small amplitude of fluctuations of ϵ demonstrates the robustness of the setup in maintaining the particles on the predefined circular trajectory defined by the modulated force.

In addition, further tests in which we varied the height from the surface (Supplementary figure 1(d)), the orbit radius R and the distance between the oscillators d (Supplementary figure 1(e)) or the amplitude of the modulation A (Supplementary figure 2) show little variations of k_r. The distributions of k_r, k_t and $k_\mathrm{B}T/\mathrm{var}(|\epsilon(\phi)|)$ also look like Gaussians (see Supplementary figure 1(f)). Hence the trap stiffness can be very well described by a harmonic potential in the range of thermal fluctuations and fairly well described by a harmonic potential up to the typical distances ϵ from the trap. In the experiments of the article, the isotropic trap stiffness k used in the theoretical model and the simulations was therefore simply measured from an individual colloidal particle trapped for 75 s in a static potential. From the independent analysis of the fluctuations of the particle in the x, y directions, plotted in Supplementary figure 1(g), and by using the equipartition theorem, we obtain the values $k_x = k_y = 4.1\,\mathrm{pN}/\mu\mathrm{m}$, and we then assume $k_r = k_t = k$.

Setting up the experimental synchronization of two rotors

Our experimental setup consists on two particles driven along a circular orbit that interact through the hydrodynamic flow induced in the viscous solvent. Supplementary figure 3(a,b) show typical trajectories of the colloidal particles and the optical traps, with $A = 0.5$ and $\delta = 3\pi/4$. Since we are applying the phase-dependent driving force $F(\phi)$, the phase angle ϕ for each rotor does not evolve at a constant rate over time. We, therefore, apply a geometrical gauge to rescale the phase $\Phi = \Phi(\phi)$ in such a way that in absence of hydrodynamic interactions, the intrinsic phase velocity is constant: $\dot{\Phi} = 2\pi/T_0 = \Omega$. The power spectrum of particle displacement during the experiment highlights that the frequencies of the particles are the same Supplementary figure 3(c).

Evaluation of the amplitude compliance

We address here the effect on the orbital radius for a rotor (that describes a circular trajectory in isolation characterized by a radius $R_{1,0}$) of a second rotor at a distance d. We consider here three force modulations: $A = 0, 0.5$ and 0.7. We recall that the two first cases lead to IP synchronization, while $A = 0.7$ leads to OP phase-locking. Supplementary figure 4(a) shows how the presence of the second rotor leads to a variation of the radius of the first rotor R_1 during an average cycle. The parameters used in the simulated trajectories are $d = 15.85\,\mu$m (two-rotors simulation) or $50\,\mu$m ("single rotor"-like), $R = 4.65\,\mu$m, $h = 10\,\mu$m, $\delta = 3\pi/4$ and $k_r = 3\,$pN$/\mu$m. Relative to the average single-rotor orbit radius $R_{1,0}$, the variations however remain small, as shown by Supplementary figure 4(b).

In Supplementary figure 4(a), the curves are very close to a sinusoidal curve of a periodicity two times smaller than the oscillator period and with a phase such that it passes through zero at $\phi = 0$, except for the OP case ($A = 0.7$). The $A = 0$ case has been explored by Niedermayer and Lenz [1], and Eq.(22) in their work shows the same features. There are however slight deviations from the expected $-\sin 2\phi$ form. First, the phase in our case is in reality slightly delayed, even for $A = 0$. We attribute this to the relaxation of the bead in the harmonic trap, that occurs with a delay of typically $6\pi\eta a/k_r$. Second, when $A = 0.5$, the oscillation starts deviating from a π-periodic sine wave. We believe this could again be due to the relaxation time in the trap: since the speed of the particle is high when $\phi \in (5\pi/4, 9\pi/4)$ because of the force modulation, ϕ evolves quickly in this region and the effect of the relaxation time leads to increased deformation of the sine wave in this range. Finally, when the amplitude is such that the oscillators do not synchronize in phase anymore, the shape experiences further deformations, as the $-\sin 2\phi$ form is only obtained for IP synchronization.

Supplementary Note 1: Further exploration of the Brownian noise and its relation with the phase slippage

Supplementary figure 5 shows an example of stochastic transition between IP and OP phase-locked states. In a particular optical tweezer experiment, we explore runs with different force modulation A. We plotted the temporal dependence of a normalised phase difference $\Delta/2\pi$. For $A = 0.5$ (resp. 0.7) and after the transient behaviour, the two rotors fluctuate around a unique value of Δ corresponding to IP (resp. OP). For $A = 0.6$, the situation is different as noise-induced switching events between IP and OP occur. The fluctuations around each phase-locked state are Gaussian

(Supplementary figure 5, bottom), indicating that the IP and OP are local stable states. To gain insight in how the noise induces hopping events between two phase-locked states, in a particular situation in which two minima are found in the potential, we show in Supplementary figure 6(a,b) the effect of the temperature on the normalised phase difference Supplementary figure 6(a) and on the resultant effective potentials (b). In Supplementary figure 6(b) the effective potentials look similar, which indicates that the fluctuations of the beads in the radial direction do not affect the shape of the effective potential, making such potentials a useful tool to characterize two-bead synchronization. In Supplementary figure 6(a), $\Delta/2\pi$ stays in a unique phase-locked state at 0 K. At 298 K, two types of events happen. First, the bead can jump between the two minima of the potential as sketched in Supplementary figure 6(b), and as can be seen on the red curve in (a). Second, bigger phase slips also occur but are less frequent (green curve in (a)). When the two types of hopping events occur, Δ can slip by more than 2π, which is illustrated by the inset of Supplementary figure 6(b). Since the potential is tilted, the bigger hopping events are highly biased towards increasing Δ.

Supplementary Note 2: Role of the height h and the angle δ

In this section, we firstly discuss further the effect of the distance to the bottom wall h in the phase-locking. h is measured by taking advantage of the fact that free particles are rather heavy and sediment quickly on the glass cover-slide that constitutes the bottom of our sample. We move the focus with the microscope stage to the equatorial plane of these particles' layer. Knowing the particles radius, this gives us the reference to measure distances above the wall. We estimate the error on this measurement to about 1 μm. It should be mentioned that the intrinsic period T_0 strongly depends on h as expected. Supplementary figure 7 shows how the intrinsic period of rotation for a single rotor describing a circular closed trajectory depends on the distance to the wall h. The straight line shows the linear dependence between T_0 and the inverse of the height. The closer to the wall, the larger the period as expected for reduced drag coefficients.

In the top panel of Supplementary figure 8 we explore the influence of h in the shape of the effective potential $V(\Delta)$. For the sake of clarity, we only compare two particular experimental conditions at moderate ($A = 0.5$) and large ($A = 0.7$) modulation parameters. Here, placing the rotors closer to the wall always leads to an OP locked-state. In the bottom panel, we consider the two limiting cases about the height explored in our setup: the lower ($3\,\mu$m) and upper ($50\,\mu$m) limits. In both situations, the shape of the potential depends on the force modulation parameter A. Though, at lower h, OP synchronised states are reached at lower values of A in comparison with what happens at larger values of h. In the latter case, only at $A = 0.9$ it is possible to reach OP.

Another interesting effect explored in this study is the role of the angle δ that sets in which position(s) along the orbit the rotors move faster. We explored three different values of δ in Supplementary figure 9. We found that for large values of A, OP locked states can be achieved.

Supplementary Note 3: Theory for the anatomy of the potential

Derivation of the coupled oscillator equation.

The position of the i-th particle ($i = 1, 2$) is

$$\mathbf{r}_i = \mathbf{r}_{i0} + R_i\mathbf{e}_{r,i} + z_i\mathbf{e}_i \tag{S2}$$

where $\mathbf{r}_{i0}$ locates the center of the trajectory, $\mathbf{e}_{r,i} = (\cos\phi_i, \sin\phi_i, 0)$ and $\mathbf{e}_i = (0, 0, 1)$ are the unit vectors in the radial and vertical directions, which constitute a moving orthogonal basis with the tangential unit vector $\mathbf{e}_{t,i} = (-\sin\phi_i, \cos\phi_i, 0)$. We will derive the equation of motion for ϕ_i up to the first order in the hydrodynamic coupling $\mathbf{G}_{ij}$ and up to the first order in the elastic compliance $\lambda_{r,t} = F_0/k_{r,t}R$, where $F_0 = \frac{1}{2\pi}\int_0^{2\pi} d\phi\, F(\phi)$ is the average driving force. A reference timescale is set by the frequency $\omega_0 = F_0/\gamma R$. Substituting the expression of the optical force

$$\mathbf{F}_i = F(\phi_i)\mathbf{e}_{t,i} - k_r(R_i - R)\mathbf{e}_{r,i} \tag{S3}$$

and the viscous drag force

$$\mathbf{g}_i = \gamma\left[\mathbf{v}(\mathbf{r}_i) - \dot{\mathbf{r}}_i\right] \simeq \gamma\left(\sum_{j\neq i}\gamma\mathbf{G}_{ij}\cdot\dot{\mathbf{r}}_j - \dot{\mathbf{r}}_i\right) \tag{S4}$$

into the equation of force balance, $\mathbf{F}_i + \mathbf{g}_i = \mathbf{0}$, we get the tangential force

$$F_{i,t} = F(\phi_i) = \gamma\left(R_i\dot{\phi}_i - \mathbf{e}_{t,i}\cdot\sum_{j\neq i}\gamma\mathbf{G}_{ij}\cdot\dot{\mathbf{r}}_j\right) \tag{S5}$$

and the radial displacement

$$\delta R_i = R_i - R = \frac{1}{k_r}\mathbf{e}_{r,i}\cdot\zeta_0[\mathbf{v}(\mathbf{r}_i) - \dot{\mathbf{r}}_i] \simeq \frac{\lambda_r}{\omega_0}\mathbf{v}(\mathbf{r}_i)\cdot\mathbf{e}_{r,i}, \tag{S6}$$

Here we used $\dot{\mathbf{r}}_i = R_i\dot{\phi}_i\mathbf{n}_i + \dot{r}_i\mathbf{e}_{t,i} + \dot{z}_i\mathbf{e}_i$ and neglected an $O(\lambda_r\lambda_t)$ term arising from $\dot{r}_i = O(\lambda_r)$. The phase velocity is obtained from Eq.(S5) as

$$\dot{\phi}_i = \left(1 + \frac{\delta R_i}{R}\right)^{-1}\left[\frac{F(\phi_i)}{\gamma R} + \frac{1}{R}\mathbf{e}_{t,i}\cdot\sum_{j\neq i}\gamma\mathbf{G}_{ij}\cdot\dot{\mathbf{r}}_j\right], \tag{S7}$$

from which we get the intrinsic phase velocity as $\omega_i = F(\phi_i)/\gamma R$ by setting $\mathbf{G}_{ij} = 0$ and $\delta R_i = 0$ (Note that we tune the trajectory of the optical trap such that an uncoupled particle follows the unperturbed circular trajectory).We can use $\dot{\mathbf{r}}_j \simeq R\omega_j\mathbf{e}_{t,j}$ in the second term in the square bracket in Eq.(S7), because the radial and vertical velocities are of $O(G_{ij})$ and make higher order contributions. We can also use $\mathbf{v}(\mathbf{r}_i) = \sum_{j\neq i}\mathbf{G}_{ij}\cdot R\omega_j\mathbf{e}_{t,j}$ in Eq.($S6$) to evaluate δR_i up to $O(\lambda_{r,t})$. Putting Eq.(S6) into (S7) with these approximations, expanding the product and retaining $O(\lambda_{r,t})$ terms, we obtain Eq. 4 in a straightforward manner.

Decomposition of the potential.

In Supplementary figure 10, we plot the effective potential decomposed according to Eq. 8, for the IP and OP cases shown in Figure 3(c,d). In both cases, we see that the flexibility-induced part (V_λ) favors in-phase synchronization, while the force-modulation part (V_A) and the cross-coupling part (V_{cross}) have out-of-phase minima. It is therefore the relative magnitude of the three parts that determines whether the IP or OP state is reached in the dynamical equilibrium.

Supplementary Note 4: Numerical simulation

The hydrodynamic coupling between two externally driven spherical particles at low Re is described by a relation between the forces acting on the colloids and the resulting velocities of the form

$$\mathbf{v}_i = \sum_{j=1}^{n} \mu_{i,j} \left[\mathbf{F}_j + \mathbf{f}_j(t)\right], \tag{S8}$$

where $\mathbf{v}_i$ is the velocity of the bead i, $\mathbf{F}_j$ represents the external tangential driving force acting on bead j. $\mu_{i,j}$ represents the mobility matrix describing the dynamics of the two particles in a viscous fluid in the proximity of a solid boundary with no-slip boundary conditions (Blake tensor). Finally, $\mathbf{f}_j$ is the stochastic Brownian noise acting on bead j. The thermal noise has zero mean $\langle \mathbf{f}_j(t)\rangle = 0$, and correlation $\langle f_j(t) f_j(t')\rangle = 2k_B T \mu_{i,j}^{-1} \delta(t-t')$ in each component, consistent with equipartition [2, 3].

The theoretical calculations and experiments with feedback-controlled optical tweezers has been compared with stochastic Brownian dynamics simulations including hydrodynamics interactions through the Blake tensor corrected for finite size particles. It describes the interaction between spheres in a semi-infinite fluid with a no-slip boundary condition at the surface. In our experiments, we only consider trajectories in the xy plane with $d \geq h$ and $d > R$ for rotors being suspended at a height h from a flat substrate placed at $z = h = 0$.

For the diagonal terms of the mobility matrix $\mu_{i,i}$, the existence of the surface changes the Stokes drag. It can be expanded as a series in a/z_i with $\mathbf{e}_z$ normal to the surface in a cartesian system of coordinates. The corresponding diagonal terms read:

$$\begin{aligned} \mu_{i,i}^{x,x} = \mu_{i,i}^{y,y} &= \frac{1}{6\pi\eta a}\left[1 - \frac{9a}{16z_i} + \frac{1}{8}\left(\frac{a}{z_i}\right)^3 - \frac{1}{16}\left(\frac{a}{z_i}\right)^5\right] \\ \mu_{i,i}^{z,z} &= \frac{1}{6\pi\eta a}\left[1 - \frac{9a}{8z_i} + \frac{1}{2}\left(\frac{a}{z_i}\right)^3 - \frac{1}{8}\left(\frac{a}{z_i}\right)^5\right] \\ \mu_{i,i}^{\alpha,\beta} &= 0\, for,\ \alpha \neq \beta. \end{aligned} \tag{S9}$$

Blake proposed in [4] to describe the fluid flow created by a Stokeslet near a surface by an image method (as in electrostatics). The no-slip boundary condition at the wall is satisfied by describing the effect of the wall as equivalent to an infinite fluid, but with a Stokeslet at the mirror position of the first Stokeslet and with an opposite force. For N particles, this leads to the following expressions for the Blake mobility matrix:

$$\mu^B_{i,j} = \frac{1}{8\pi\eta}\left[\mathbf{G}^S(\mathbf{r}_i - \mathbf{r}_j) - \mathbf{G}^S(\mathbf{r}_i - \overline{\mathbf{r}}_j) + 2z_j^2\mathbf{G}^D(\mathbf{r}_i - \overline{\mathbf{r}}_j) - +2z_j\mathbf{G}^{SD}(\mathbf{r}_i - \overline{\mathbf{r}}_j)\right], \tag{S10}$$

with $\mathbf{r}_i = (x_i, y_i, z_i)$, $\overline{\mathbf{r}}_i = (x_i, y_i, -z_i)$, and with the elements of the Green functions given by [4].

$$\begin{aligned}
\mathbf{G}^S_{\alpha,\beta}(\mathbf{r}) &= \frac{\delta_{\alpha,\beta}}{r} + \frac{r_\alpha r_\beta}{r^3} \\
\mathbf{G}^D_{\alpha,\beta}(\mathbf{r}) &= (1 - 2\delta_{\beta,z})\frac{\partial}{\partial r_\beta}\left(\frac{r_\alpha}{r^3}\right) \\
\mathbf{G}^{SS}_{\alpha,\beta}(\mathbf{r}) &= (1 - 2\delta_{\beta,z})\frac{\partial}{\partial r_\beta}\mathbf{G}^S_{\alpha,z}(\mathbf{r}),
\end{aligned} \tag{S11}$$

with δ the Kronecker delta.

Supplementary References

[1] Niedermayer, T., Eckhardt, B. & Lenz, P. Synchronization, phase locking, and metachronal wave formation in ciliary chains. *Chaos* **18**, 037128 (2008).

[2] Doi, M. & Edwards, S. F. *The Theory of Polymer Dynamics* (Oxford University Press, New York, 1986).

[3] Bruot, N. & Cicuta, P. Realizing the physics of motile cilia synchronization with driven colloids. *Annu. Rev. Condens. Matter Phys.* **7**, 1–26 (2016).

[4] Blake, J. R. A note on the image system for a stokeslet in a no-slip boundary. *Math. Proc. Camb. Phil. Soc.* **70**, 303–310 (1971).